Influence of Disorder in High-Entropy Alloys on Thermoelectric Properties and Phase Stability

Ming Xia, Marie-Christine Record, Pascal Boulet

Influence of disorder in high-entropy alloys on thermoelectric properties and phase stability

Ming Xia, Marie-Christine Record, Pascal Boulet*

Ming Xia, Aix-Marseille University, Faculty of Sciences, Department of Chemistry, avenue normandie-Niemen, F-13013 Marseille, France

Marie-Christine Record, Aix-Marseille University, Faculty of Sciences, Department of Chemistry, avenue normandie-Niemen, F-13013 Marseille, France

Pascal Boulet, Aix-Marseille University, Faculty of Sciences, Department of Chemistry, avenue normandie-Niemen, F-13013 Marseille, France

Keywords: High-entropy alloys, thermoelectricity, density functional theory, chalcogenides

ABSTRACT. High-entropy alloys (HEA) are characterized by a multi-element composition and extensive atomic mixing. To explore the impact of disorder in PbSnTeSe HEA on its thermoelectric (TE) properties and phase stability, we have built two structurally ordered alloys with the same composition as that of the disordered one. Ordered alloys have been designed by artificially setting the positions of the atoms so that they form a symmetrical structure rather than a completely random structure. The symmetrical alloys have a tetragonal structure and an

orthorhombic one. It is found that, all the structures are mechanically stable while only the HEA is dynamically stable. The Multi-Cell Monte Carlo algorithm $(MC)^2$ predicts a single phase of the HEA, which is consistent with the literature experimental results. The analysis of free energy shows that the HEA has the lowest values. These results suggest that HEA is more stable than the two symmetrical structures emphasizing the role of atomic disorder in the stability of high-entropy alloys. Utilizing first-principles density-functional theory (DFT) and Boltzmann transport theory, the thermoelectric transport properties of these symmetrical structures have been analyzed and compared to those of the disordered structure. The results indicate small optimal-value differences in the Seebeck coefficient S. The optimal values of S are approximately 180 μV/K, except for the n-type ORTH, for which S is only 100 μV/K. The electrical conductivity of ORTH and TET increases compared to that of HEA. For a temperature of 300 K and a carrier concentration of 10^{21} cm^{-3}, the n-type conductivity increases from 75×10^5 S/m for HEA to 110×10^5 S/m and 120×10^5 S/m for ORTH and TET; the p-type conductivity increases from 5.5×10^5 S/m for HEA to 16×10^5 S/m and 17×10^5 S/m for ORTH and TET. The lattice thermal conductivities determined by the Green-Kubo formalism are similar for both the HEA and the two ordered structures. This suggests that the low thermal conductivity in high-entropy alloys primarily stems from multi-element composition, with atomic disorder playing a minor role. Based on the electronic and thermal transport coefficients, the figure of merit ZT values have been determined. Compared to HEA, the optimal ZT value of the n-type ORTH and TET decreases, but for the p-type doping, the ZT value increases from 0.75 for HEA to 1.1 for both TET and ORTH.

INTRODUCTION

In the past few years, the current global energy crisis and greenhouse effect has become increasingly severe. Thermoelectric materials have garnered wide interest due to their ability to

directly transform waste heat into electrical energy[1–4]. The figure of merit $ZT = S^2\sigma T/\kappa$ is used to evaluate the thermoelectric conversion efficiency where S, σ, T, and κ are the Seebeck coefficient, electrical conductivity, temperature, and thermal conductivity (electronic and lattice), respectively. Nevertheless, improving thermoelectric efficiency is challenging owing to the strong coupling among these parameters[2]. Hence, several strategies have been developed to improve the TE properties, such as doping[5], nanostructuring[6–8], reducing the dimensionality[9–11], applying strains[12], etc. Apart from enhancing the thermoelectric efficiency of current materials through these strategies, the exploration of new thermoelectric materials is also a crucial way[13].

In recent years, high-entropy alloys have attracted lots of attention in the field of materials science[14–19]. They have been investigated for mechanical[20], catalytic[21], photocatalytic[22], and refractory properties[23], etc. High entropy alloys are typically defined as a solid solution with five or more principal elements, each in a 5 to 35% molar ratio, resulting in high configurational mixing entropy (S_{conf}), defined as $S_{conf} = -k_B \sum_{i=1}^{N} x_i ln(x_i)$ where x_i is the molar fraction for each element $i = 1, \dots, N$ with N the number of elements[14]. It is generally admitted that the high entropy of mixing favors the formation of solid solutions and reduces the number of phases[14]. High-entropy alloys are known to have four major effects: high-entropy effect, lattice distortion effect, slow diffusion effect, and "cocktail" effect[14]. Due to the lattice distortion effects[24], which reduce phonon velocity and enhance the scattering of phonons, high-entropy alloys typically exhibit low lattice thermal conductivity[25–27], which have made them attractive for thermoelectric applications. It has been reported that the high-entropy metal chalcogenide (Ag,Pb,Bi)(S,Se,Te) alloy with a NaCl-type structure is a n-type semiconductor with very low κ_l and good power factor ($PF = S^2\sigma$) resulting in a figure of merit of 0.54 at 723 K[28]. The ZT value of a n-type PbSe-based high-entropy material formed by entropy-driven structural stabilization was found to be 1.8 at 900 K, which

corresponds to a material with excellent thermoelectric properties[29]. Recently, PbSnTeSe has been experimentally investigated for the thermoelectric properties by Fan et al.[30] and Raphel et al[31,32]. Since PbSnTeSe has been experimentally proved to be single phased, the present study has been focussed on this compound. PbTe crystallizes in a NaCl-type structure. PbSnTeSe is formed by replacing some Pb and Te atoms with Sn and Se atoms. This substitution creates chemical disorder, which increases phonon scattering due to fluctuations in atomic radii, thereby reducing thermal conductivity. Despite this disorder, the mobility of charge carriers remains largely unaffected because the crystal lattice is preserved. As a result, high entropy alloys are expected to meet the "phonon-glass electron-crystal" criterion essential for efficient thermoelectric material[33]. Unlike thermal conductivity, the Seebeck coefficient varies inversely with electrical conductivity. A common approach to enhance the power factor ($S^2\sigma$) is through band engineering, such as atom substitution within the compound. While most compounds have limited solubility for foreign element in their crystal structures, high entropy alloys inherently possess this solubility. In the majority of studies on high entropy alloys for thermoelectric applications, the focus has been on enhancing the thermoelectric properties of the materials[34-47]. However, no studies have investigated whether the transport properties in high entropy alloys are primarily influenced by the disorder or by the larger number of varied chemical elements present. This computational work aims to address this question.

In a previous study, we presented a complete approach to obtain all the thermoelectric transport coefficients and investigated the thermoelectric transport properties of the PbSnTeSe high-entropy alloy[48]. The HEA typically features a multi-element composition and high atomic mixing[14,49]. In the present investigation, to study the effects of disorder of HEA on the thermoelectric properties and phase stability, we have built two structurally ordered PbSnTeSe alloys with the same

composition as that of the HEA by choosing the atomic positions in a way to form a symmetrical structure instead of a completely random one. Two symmetrical alloys have then been formed: a tetragonal structure with space group Pmmm (hereafter called TET) and an orthorhombic structure with space group P4/mmm (hereafter called ORTH).

The dynamical and mechanical stabilities of the HEA and symmetrical structures have been investigated, and the stability of the HEA with respect to phase separation have been studied using the multi-cell Monte Carlo relaxation method[50]. The thermoelectric transport properties of the two symmetrical structures (TET and ORTH) have been investigated by combining first principles density-functional theory with the Boltzmann transport theory for the electronic part. Ab initio molecular dynamics (AIMD)[51] simulations combined with on-the-fly development of a machine-learned force field (MLFF)[52-54] have been used to investigate the lattice thermal conductivity of the structures.

COMPUTATIONAL METHODS

First-principles calculations have been performed by using density functional theory[55,56] with the Perdew–Burke–Ernzerhof functional (PBE)[57] and projector augmented waves (PAW) as implemented in the Vienna Ab initio Simulation Package (VASP) code[51,58,59]. A 8×8×8 Monkhorst-Pack k-point mesh has been used, and the kinetic energy cutoff has been set to 500 eV for the HEA, ORTH and TET. During structural relaxation, the energy and force convergence criteria have been set to 1×10^{-8} eV and 1×10^{-5} eV/Å, respectively. The electronic transport properties have been calculated by employing the semi-classical Boltzmann theory within the relaxation time approximation (RTA) with the BoltzTraP2 code[60]. The energy eigenvalues given to BoltzTraP2 have been calculated with the VASP code using a dense 21×21×21 k-point mesh. Since the compositions are the same for all the structures, the electron relaxation time of the HEA[48] is

adopted for both TET and ORTH. Because of the presence of heavy Te and Se atoms, the spin-orbit coupling (SOC) effect has been considered in our calculations.

Ab initio molecular dynamics (AIMD)[51] simulations combined with on-the-fly development of a machine-learned force field (MLFF)[52-54] have been used to investigate the lattice thermal conductivity of the structures at different temperatures, in which a 4×4×4 (resp., 4×4×8) supercell (512 atoms) has been employed for ORTH (resp., TET). The lattice thermal conductivity has been calculated from the Green–Kubo theory by accumulating the heat flux during the simulations. For the AIMD simulations of TET and ORTH, the adopted force field was that of the HEA developed in our previous investigation[48]. This approximation should be reasonable since, given the wide variety of types of bonds in the HEA, those present in TET and ORTH structures must be found there as well. First, the force field has been used to equilibrate the system in the NVT ensemble at the desired temperature with a time step of 1 fs for 100 ps long. After the system was equilibrated, the force field has been used to obtain the heat flux in the NVE ensemble with a time step of 1 fs for 100 ps long. For ensemble average purpose, 10 independent molecular dynamics simulations have been performed for the calculation of the heat flux. The phonon spectra have been calculated employing 2×2×2 supercells with the Phonopy Package[61] using the finite displacement method with the MLFF.

For the $(MC)^2$ simulation of HEA, a cutoff energy of 400 eV and a k-point mesh of 1 × 1 × 1 have been used. The electronic and ionic convergence criteria have been set to 1×10^{-4}eV and 0.05 eV/Å, respectively.

RESULTS AND DISCUSSION

Structural properties. The PbSnTeSe HEA structure has been built from the PbTe crystal structure for which the same atomic ratio of 50% has been employed for both Pb and Sn on the Pb

Wyckoff position, and Te and Se on the Te Wyckoff position. Fig. 1(a) shows the schematic illustration of the crystal structure of the PbSnTeSe HEA. Fig. 1(b) is a 2×2×2 supercell containing 64 atoms and shows the special quasi-random structure (SQS) of PbSnTeSe high entropy alloy generated by the MCSQS tool of ATAT[62]. Generally, high-entropy alloys are fully disordered with high entropy effects due to the multi-element components. To study the effects of disorder of the HEA on the thermoelectric properties and phase stability, we have artificially set Sn and Se atoms in a multicell lattice of PbTe in a way to obtain symmetrical structures with same composition as that of the HEA. The symmetrical alloys have a tetragonal structure with space group Pmmm and an orthorhombic structure with space group P4/mmm, respectively, as shown in Fig. 1(c) and Fig. 1(d). As a shortcut, we will refer to the tetragonal structures as "TET" and orthorhombic structure as "ORTH" respectively. The optimized lattice parameters of the TET are a = 4.48 Å, b = 4.48 Å and c = 6.31 Å, $\alpha = 90.0°$, $\beta = 90.0°$ and $\gamma = 90.0°$, and the optimized lattice parameters of the ORTH are a = 6.32 Å, b = 6.32 Å and c = 6.32 Å, $\alpha = 90.0°$, $\beta = 90.0°$ and $\gamma = 90.0°$.

Stability of the alloys. The stability of the symmetrical TET and ORTH structures has been explored and compared to that of the HEA. Both the zero-Kelvin mechanical and dynamical stabilities have been investigated by calculating the elastic constants and phonon dispersion curves, respectively. Additionally, the thermodynamic functions have been calculated to shed light on the relative stability of the alloys at finite temperatures. And the stability of the HEA against decomposition has been investigated.

Mechanical stability. The elastic constants of the three structures are presented in Table 1. Due to the absence of symmetry elements in the lattice of the HEA structure (P1 space group), the HEA has 21 independent elastic constants. Since the symmetry of ORTH and TET is orthorhombic and

tetragonal I, respectively, their mechanical response can be described by 9 independent elastic constants for the former while by 6 ones for the later[63].

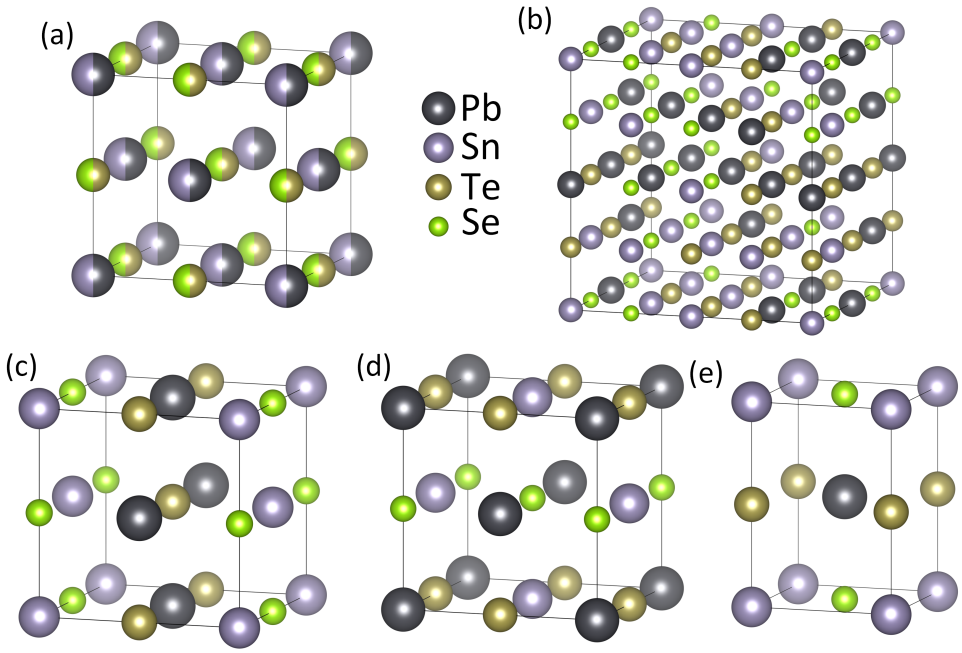

Figure 1. (a) Schematic view of the crystal structure of PbSnTeSe. (b) HEA generated by ATAT-MCSQS method. (c) Alloy of tetragonal structure. (d) Alloy of orthorhombic structure. (e) Primitive cell of tetragonal structure.

Table 1. Calculated elastic constants (in GPa) of HEA, ORTH and TET.

	C_{11}	C_{12}	C_{13}	C_{14}	C_{15}	C_{16}	C_{22}	C_{23}	C_{24}	C_{25}	C_{26}
HEA	67.64	12.11	4.89	0.42	0.90	1.81	77.15	7.97	-1.72	0.30	5.69
ORTH	116.0	7.25	7.55				116.0	7.68			
TET	77.11	45.28	7.79				77.11	7.79			
	C_{33}	C_{34}	C_{35}	C_{36}	C_{44}	C_{45}	C_{46}	C_{55}	C_{56}	C_{66}	
HEA	79.49	-2.10	2.71	-0.48	13.11	0.90	0.30	7.78	0.05	12.33	
ORTH	115.4				15.77			15.75		16.36	
TET	116.7				15.95			15.95		52.65	

The mechanical stability can be evaluated by the famous Born-Huang standard relations[63]. Born's criteria for an orthorhombic system are:

$$C_{11} > 0$$

$$C_{11}C_{22} > C_{12}^2$$

$$C_{11}C_{22}C_{33} + 2C_{12}C_{13}C_{23} - C_{11}C_{23}^2 - C_{22}C_{13}^2 - C_{33}C_{12}^2 > 0$$

$$C_{44} > 0, C_{55} > 0, C_{66} > 0$$

For the elastic stability in the tetragonal I case, these relations are:

$$C_{11} > |C_{12}|$$

$$2C_{13}^2 < C_{33}(C_{11} + C_{12})$$

$$C_{44} > 0, C_{66} > 0$$

According to Table 1, the elastic constants of all the structures meet the criteria for mechanical stability, indicating that they are all mechanically stable. The average mechanical properties of bulk crystals can be obtained from the Voigt[64], Reuss[65] and Hill[66] methods. Based on the calculated bulk modulus B and shear modulus G, the Young modulus Y and Poisson's ratio σ can be determined by:

$$Y = \frac{9BG}{3B + G}$$

$$\sigma = \frac{(3B - 2G)}{2(3B + G)}$$

Table 2 reports the bulk modulus, the shear modulus, the Young modulus and the Poisson ratio of the three structures. The bulk and shear moduli and Poisson's ratio of ORTH and TET are very comparable indicating that their mechanical behavior is also comparable. For instance, the Pugh ratio B/G (1.63 and 1.64), and Poisson ratio (0.24) of ORTH and TET indicate that they both are

brittle (B/G<1.75 and ν <0.26). However, the Cauchy pressure C_{12}-C_{44} yields contradictory information: a negative value indicates a brittle material, which is the case for ORTH, whereas a positive value indicates a ductile material, which is verified for TET. It is noted that the bulk, shear and Young moduli values of ORTH and TET are greater than those of HEA, whereas the opposite occurs for the Poisson ratio, all suggesting that HEA is more prone to deformations than ORTH and TET.

Table 2. Calculated bulk modulus B, shear modulus G, Young's modulus Y (in GPa) and Poisson's ratio σ of HEA, ORTH and TET. The subscripts represent the Voigt, Reuss and Hill method respectively.

	B_V	B_R	B_H	G_V	G_R	G_H	Y_V	Y_R	Y_H	σ_V	σ_R	σ_H
HEA	30.47	29.57	30.02	19.94	14.08	17.01	49.10	36.46	42.92	0.23	0.29	0.26
ORTH	43.59	43.59	43.59	31.24	22.23	26.73	75.64	57.00	66.59	0.21	0.28	0.24
TET	43.62	43.62	43.62	30.91	22.15	26.53	75.01	56.83	66.17	0.21	0.28	0.24

Dynamical stability. The phonon dispersion relations of the HEA and ORTH and TET have been calculated and depicted in Fig. 2. For the HEA, there are 192 phonon bands due to a total of 64 atoms. It is shown that the maximum frequency of the phonon bands is not much different in the three structures and lies around 4 THz. Among the three structures, only the HEA has no imaginary frequency, and both the ORTH and TET exhibit phonon bands expanding across the Brillouin zone with large imaginary frequencies. It indicates that only the HEA is dynamically stable whereas both the ORTH and TET lack such stability. This result infers that the atomic disorder makes a significant contribution to the dynamic stability of high entropy alloys.

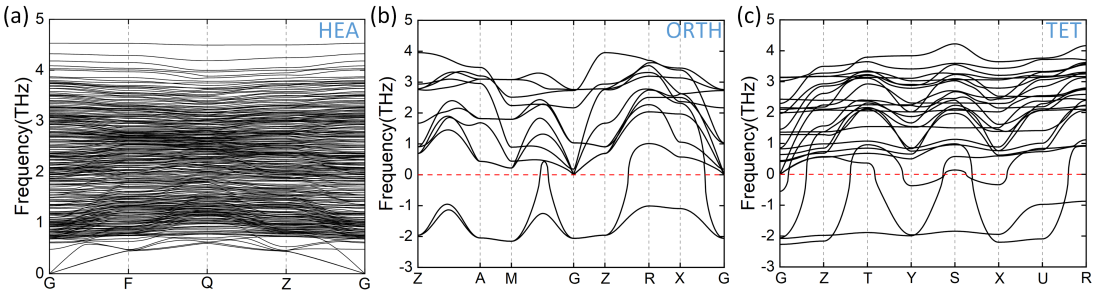

Fig. 2 Calculated phonon spectra of HEA (a), ORTH (b) and TET (c).

Thermodynamic stability. *a) Thermodynamic state functions*. To investigate the stability at finite temperatures, the evolution of the electronic energy, vibrational energy, and total energy with temperature have been calculated (Fig. 3). By utilizing the adiabatic free energy decomposition, the Helmholtz free-energy F(T) in a system at temperature T can be approximated as[49]:

$$F(T) = E + F_{el}(T) + F_{vib}(T) - TS_{conf}$$

E is the total electronic energy of the structure with all the atoms relaxed to their T = 0 K equilibrium position, S_{conf} is the chemical configurational entropy, $F_{el}(T)$ is the free energy due to electronic excitations and $F_{vib}(T)$ is the free energy due to atomic vibrations. By using the Fermi-Dirac distribution to populate the electronic energy levels at a temperature of interest and under the fixed DOS approximation (i.e., DOS calculated at zero Kelvin), $F_{el}(T)$ can be evaluated through the relations[49]:

$$F_{el}(T) = U_{el}(T) - TS_{el}(T)$$

$$U_{el}(T) = \int_{-\infty}^{\infty} D(\varepsilon)\, f(T)\varepsilon d\varepsilon - \int_{-\infty}^{\varepsilon_F} D(\varepsilon)\, \varepsilon d\varepsilon$$

$$S_{el}(T) = k_B \int_{-\infty}^{\infty} D(\varepsilon) s(\varepsilon, T) d\varepsilon$$

$$s(\varepsilon, T) = -[f \ln(f) + (1-f)\ln(1-f)]$$

In these relations, $f = f(\varepsilon, T)$ is the Fermi-Dirac distribution function, ε_F the zero-temperature Fermi energy and the terms in $s(\varepsilon, T)$ stand for a temperature-weighted configurational entropy contribution due to the creation of electrons and holes. We note that, in the above formulation we use the so-called fixed DOS approximation $D(\varepsilon)$ since the dependence of the DOS and of the electronic energy levels with the volume change upon temperature increase (i.e., thermal expansion) is neglected.

The free energy contribution due to atomic vibrations can be large and can strongly impact phase stabilities. The quasi-harmonic approximation is employed to obtain an accurate description of the vibrational free energy. In this approximation, the vibrational free energy reads[49]:

$$F_{vib}(T) = \frac{1}{N}\sum_{j}^{3N}\left\{\frac{1}{2}\hbar\omega_j + k_B T \ln\left[1 - \exp\left(-\frac{\hbar\omega_j}{k_B T}\right)\right]\right\}$$

where $\hbar$ is the reduced Planck constant and the ω_j are phonon frequencies. The sum runs over the $3N$ frequencies for a lattice containing N atoms. In general, two well established approaches exist to compute the ω_j, the linear response theory and the finite-displacement supercell method.

The configurational entropy assumes a crucial role in disordered multicomponent phases such as in HEA characterized by elevated concentrations of elements. For ordered phases, $S_{conf} = 0$. A reasonable approximation for the configurational entropy of a fully disordered system is to assume an ideal mixing behavior (i.e., no short range order)[49]:

$$S_{conf} = -k_B \sum_{\mathrm{i=1}}^{\mathrm{N}} x_i ln(x_i)$$

where x_i is the molar fractions for each element $i = 1, \ldots, N$ with N the number of elements.

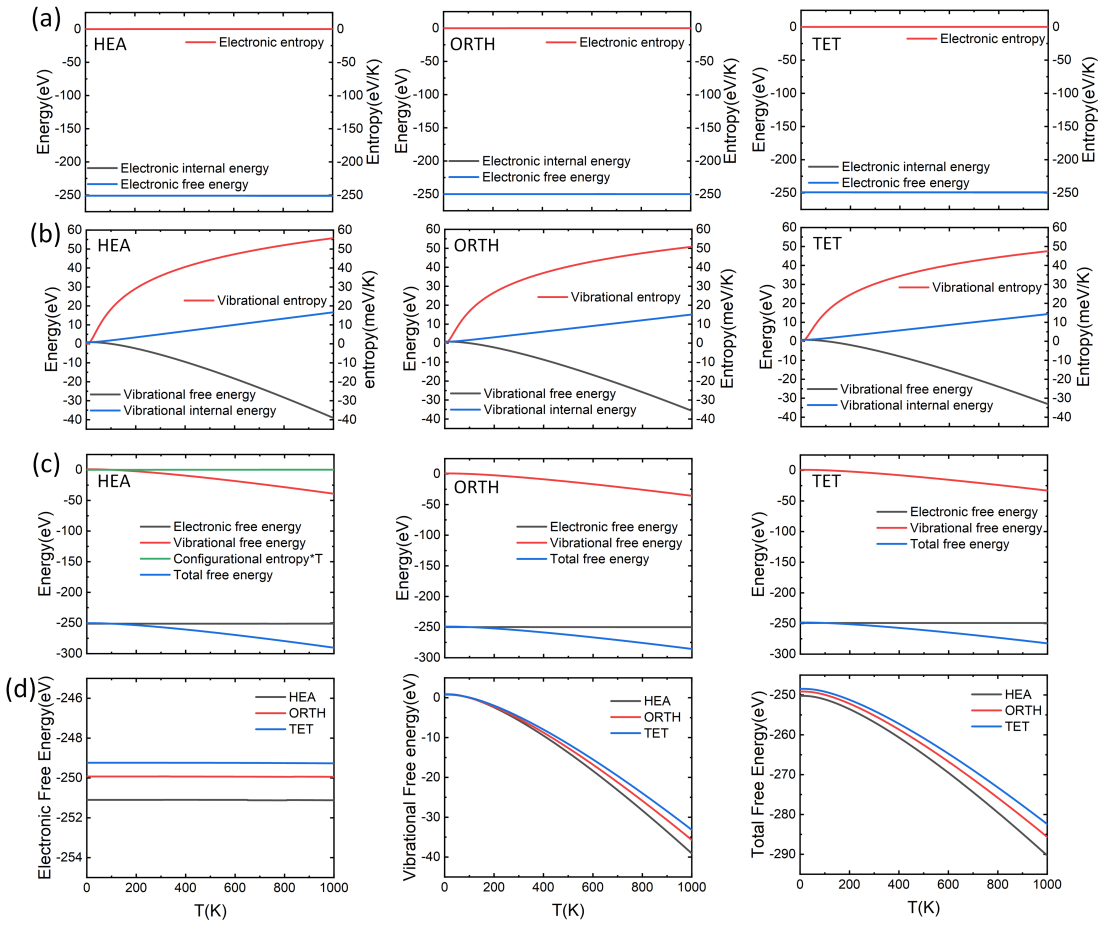

Figure 3. Electronic energy (a), vibrational energy (b), and total energy (c) of HEA, ORTH and TET as a function of temperature. Comparison of the electronic free energy, the vibrational free energy, and the total free energy for HEA, ORTH and TET(d).

Fig. 3(a) shows the electronic internal energy, electronic entropy, and electronic free energy as a function of temperature for the three structures. It is shown that the value of the electronic entropy for all the structures is very small, in fact almost null, irrespective of the temperature. Thus, the electronic free energy changes little with the temperature (in Fig. 3a, $U_{el}(T)$ and $F_{el}(T)$ are quasi superimposed). The evolution of the vibrational internal energy, vibrational entropy, and vibrational free energy with the temperature of the three structures is depicted in Fig 3(b). It

indicates that the vibrational entropy and the vibrational internal energy increase with the temperature whereas the vibrational free energy decreases with temperature. Fig. 3(c) shows all the energy contributions (i.e., electronic energy, vibrational energy, and configurational energy) to the total free energy as a function of temperature. For the HEA the configurational free energy ($-S_{conf} \times T$) remains very small over the whole range of temperatures: it reaches 0.12 eV at 1000 K. The electronic free energy changes little with the temperature and the vibrational free energy decreases with temperature for all the structures. A comparison of the electronic, vibrational and total energies between the three structures is given in Fig. 3(d). It shows that the HEA bears the lowest total free energy on the whole range of temperatures, followed by ORTH and then TET. Hence, the order of stability is HEA, which is about 1.5 eV more stable at 0 K than ORTH, itself more stable than TET by about 0.3 eV. As the temperature rises, the total free energies decrease suggesting that the structures are more stable at higher temperature.

b) Phase stability. In order to further investigate the stability of the PbSnTeSe HEA, the $(MC)^2$ program[35] has been used to assess whether the HEA is single phased or if a phase separation occurs. The Multi-Cell Monte Carlo algorithm, or $(MC)^2$, is especially designed for predicting stable phases or phase separations at given temperatures in chemically complex crystalline systems. This algorithm takes advantage of multiple cells to represent possible phases, while eliminating the size and concentration restrictions as in previous homologous algorithms[50]. Free atomic transfer among cells is accomplished by applying the lever rule. The transfer of random atoms is realized by changing the species of an atom in one or more cells; this Monte Carlo move is called a "flip" move. Free atomic transfer acceptance is based on the standard Monte Carlo criterion of the isothermal-isobaric ensemble (see Ref. [50]). An assigned molar ratio virtually controls the

percentage of each cell in the overall simulation, making $(MC)^2$ a successful algorithm for simulating phase coexistence in crystalline solids.

Fig. 4 depicts the results of a $(MC)^2$ run of PbSnTeSe HEA at 300 K, starting with four equiatomic random face-centered cubic (fcc) SQS cells containing 64 atoms each (16 atoms of each species). The energy drops rapidly at the beginning of the simulation (Fig. 4(c)), and after a few steps the energy stabilizes at a certain value, which indicates a convergence of the energy or concentration. Concentrations in cells 1, 2 and 4 are gradually changing, while cell 3 retains more or less an equiatomic composition (Fig. 4(a)). However, since the molar fractions of cells 1, 2 and 4 eventually become zero (Fig. 4(b)), they do not represent a phase after the overall simulation and thus are discarded by $(MC)^2$. Therefore, the only remaining phase is PbSnTeSe in cell 3 indicating that there is no phase separation after the overall simulation. Thus, the $(MC)^2$ algorithm predicts that the PbSnTeSe HEA is single phased. This prediction is consistent with the experimental results.

Electronic and transport properties. *Electronic band structures*. Due to the presence of the heavy elements Pb, Te and Sn, the spin–orbit coupling (SOC) effect has been considered for the calculation of the band structures (Fig. 5). The ORTH is a semiconductor with a direct band gap, and both the valence-band maximum (VBM) and conduction-band minimum (CBM) are located at the UR high symmetry line either with or without SOC effects, as shown in Fig. 5(a) and Fig. 5(c). The band gap increases from 0.04 eV to 0.07 eV and the energy difference between the conduction band valley and the valence band valley becomes larger when considering the SOC effects. Without spin-orbit coupling effects, the TET is also a semiconductor with a direct band gap, and the VBM and the CBM are both located at the RX high symmetry line, as shown in Fig.

5(b). The band gap increases from 0.07 eV to 0.11 eV and the band shape around the VBM and CBM changes considerably when considering the SOC effects. Indeed, without SOC, two maxima appear in the VBM region with nearly equal energies whereas the CBM is made of a single peak of minimum energy. By contrast, when considering SOC effects, the picture is somewhat inverted with a single maximum in the valence band and two minima of equal energies in the conduction band. In both cases, the band shapes around the Fermi level stem from the SOC-induced band avoided crossing. It is noteworthy that, by contrast to HEA, there is no band splitting effect caused by the spin-orbit coupling, therefore reducing the number of conduction channels compared to HEA.

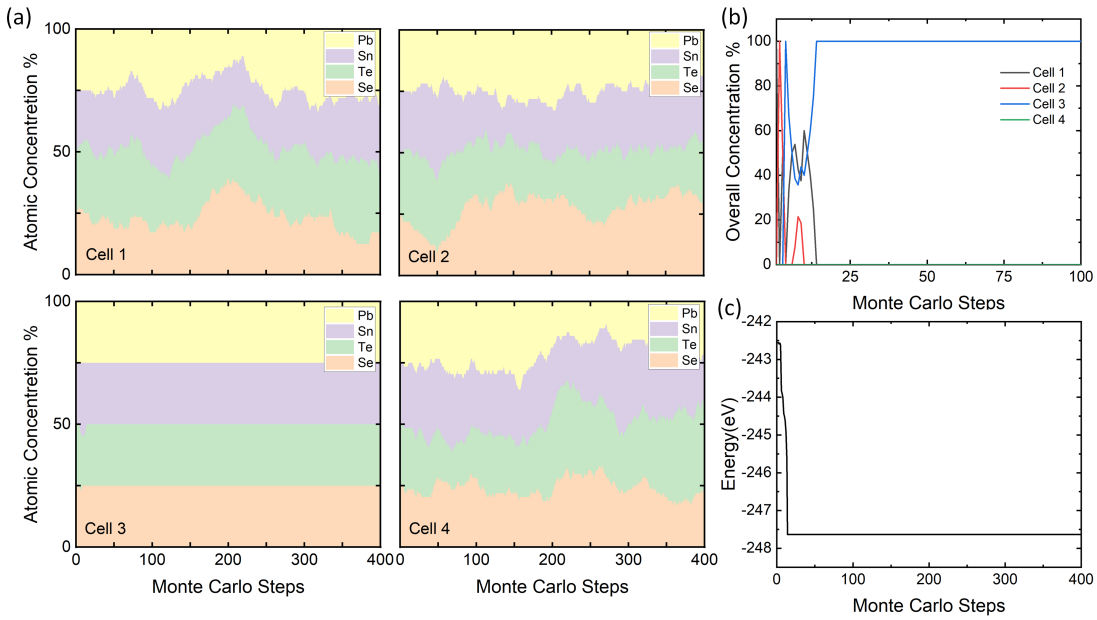

Figure 4. Evolution of (a) composition in each simulation cell, starting from the randomized PbSnTeSe structure with same equiatomic composition. (b) Molar fractions in the four cells. (c) Energy during the Monte Carlo process.

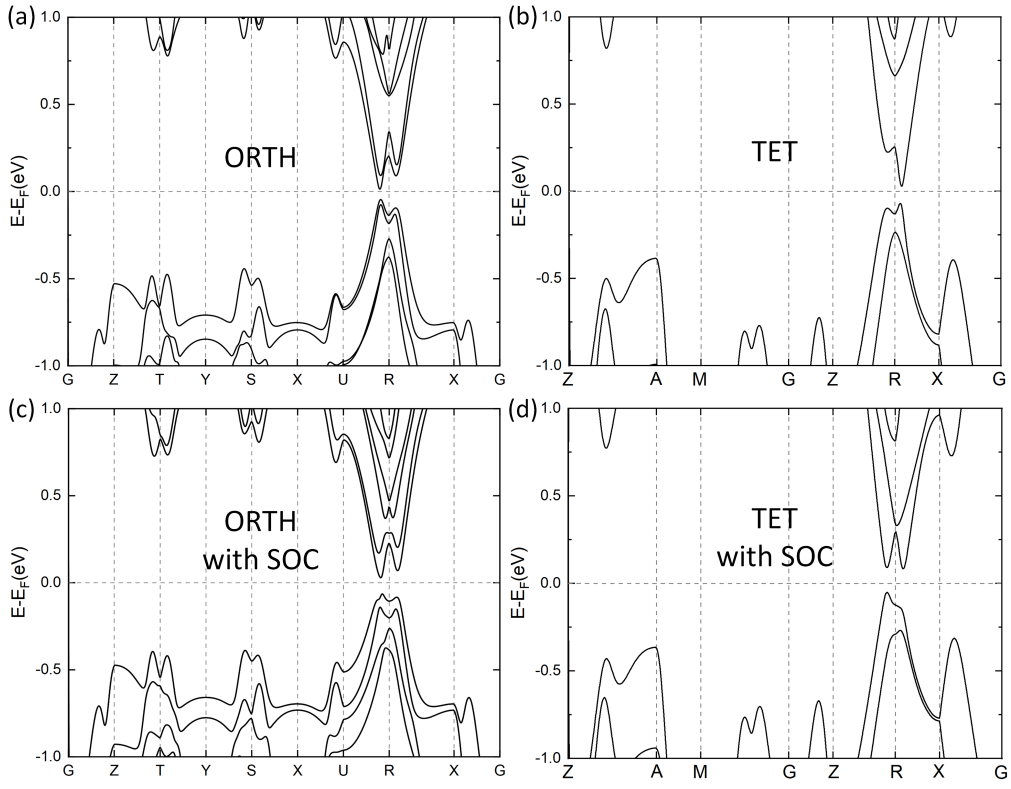

Figure 5. Calculated band structures of ORTH and TET without SOC effects (a) and (b) and with SOC effects (c) and (d).

Electronic transport properties. Fig. 6 (a) shows the Seebeck coefficient (*S*) of the TET and ORTH structures as a function of the charge carrier concentration at the temperatures of 300 K, 500 K, and 700 K. As can be seen, the Seebeck coefficients of TET and ORTH increase first and then decrease. At low charge carrier (electron or hole) concentrations, *S* increases very slowly (in absolute value); this behavior is caused by a bipolar effect itself due to the intrinsic excitation[67]. Intrinsic excitation usually occurs in narrow band gap materials, lower doping carrier concentration regions and at high temperatures altogether. After a given carrier concentration is reached, the Seebeck coefficient increases steeply to reach a maximum that increases with temperature for the ORTH, irrespective of the carrier type. For the n-type case, the Seebeck coefficient of TET is larger than that of ORTH, which results from the presence of the two

conduction band valleys in TET and a smaller bandgap of ORTH. For the case of p-type doping, there is little difference in the Seebeck coefficient between ORTH and TET except for the temperature of 300 K for which the TET structure exhibits a broad and high peak at 10^{19} holes/cm^3 while ORTH bears small S values. We note that the p-type ORTH exhibits peak values of S at high doping level only, irrespective of the temperature, a behavior that may stem from the very small bandgap of the structure. Compared with HEA[48], there is little difference in the behavior of the Seebeck coefficient with the n-type TET, S of TET being smaller than that of HEA. The behavior of S for the p-type TET and the n- and p-type of ORTH are obviously different from that of HEA, especially with respect to the concentration of charge carriers as the HEA Seebeck coefficient decreases in magnitude with increasing doping concentration and the maximum is shifted towards higher concentrations as the temperature increases. We observe markedly different behaviors in Fig. 6(a). The difference in the maxima of Seebeck coefficients between HEA, and ORTH and TET can be explained from the band structures. In HEA, the electronic bands near the VBM and CBM are relatively flat. This results in a high density of states and a high corresponding derivative near the Fermi level, which is favorable for a high Seebeck coefficient. In contrast, the electronic bands of ORTH and TET are quite stiff near the Fermi level, leading to a somewhat lower S. However, for n-type TET, a band degeneracy and two-fold minimum of the conduction band compensate the decrease of S. For p-type ORTH and TET this compensation can be related to a two-fold maximum and a band degeneracy, respectively, of the valence band.

For TET and ORTH, we have adopted the same electron relaxation time values, one for the n-type and one for the p-type conduction, as those of the fully disordered HEA due to the identical composition of the three structures. Fig. 6(b) shows the electrical conductivity (σ) of the two structures as a function of the carrier concentration at the temperatures of 300 K, 500 K and 700

K. The electrical conductivity of both TET and ORTH increases with the carrier concentration and decreases with the temperature at the higher carrier concentration, the latter suggesting a degenerate semiconductor behavior. The flat curve of σ at low carrier concentrations is reminiscent of the bipolar effect. For both structures, the electrical conductivity of n-type conduction is always larger than that of p-type one, which can be explained by the larger relaxation time for the n-type carriers than for the p-type ones. Indeed, at the temperatures of 300 K, 500 K, and 700 K, the relaxation times for n-type and p-type HEA PbSnTeSe vary from 158 to 44.3 fs and from 17.3 to 4.78 fs, respectively (see Ref. [48]). Compared with HEA[48], for both n-type and p-type doped TET and ORTH structures, the electrical conductivity is increased. The band structure features can explain these differences. For ORTH and TET, the electronic bands are quite stiff near the VBM and CBM, which results in a low mass of the charge carriers. Consequently, the carrier mobility is high, which, according to the Drude-Sommerfeld model, explains the higher electrical conductivity of ORTH and TET compared to HEA. The increased band degeneracy observed in the ORTH and TET, which increases the effective mass of the carriers, should counteract this phenomenon. However, this increased degeneracy is obviously not strong enough to lower the electrical conductivity below that of the HEA.

Fig. 6(c) shows the power factor ($PF = S^2\sigma$) of the two structures as a function of the carrier concentration at the temperatures of 300 K, 500 K and 700 K. For both ORTH and TET, the power factor of n-type doped structures is larger than that of p-type ones, which is due to the higher electrical conductivity in the case of n-type conduction. Compared to n-type structures, the optimal value of the power factor in p-type ones shifts to higher carrier concentration.

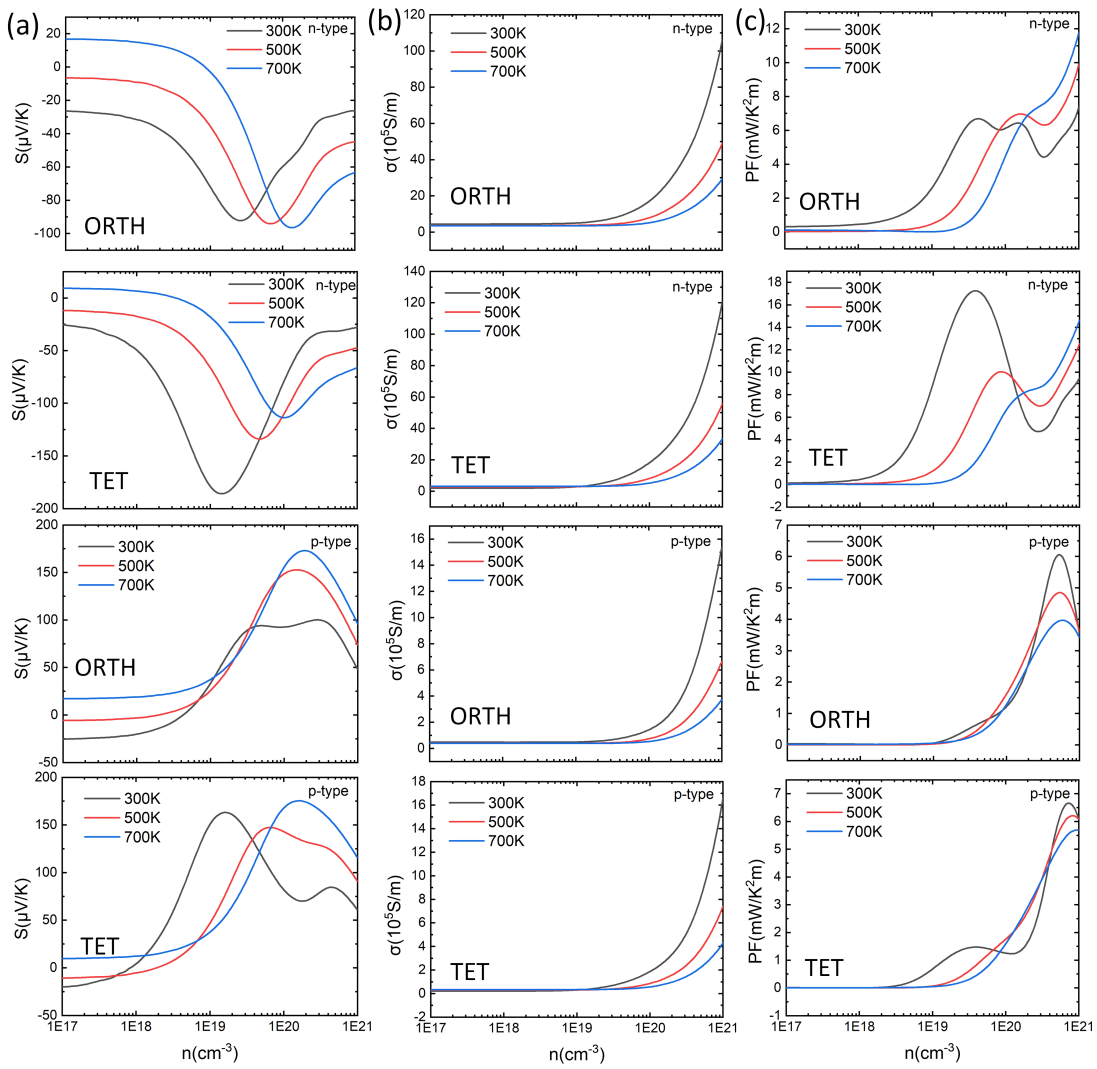

Figure 6. Seebeck coefficient (S) (a), electrical conductivity (σ) (b), and power factor (PF) (c) of ORTH and TET for n-type and p-type at 300 K, 500 K, and 700 K as a function of carrier concentration.

The power factor of the HEA[48] exhibits about the same maximal values in the doping range 5×10^{19}-5×10^{20} carriers/cm^3, irrespective of the temperature. Comparing the n-doped structures, TET bears a higher power factor and ORTH a lower one than HEA. For the p-type structures, the power factor of both symmetrical ones is improved, though at much higher carrier concentrations.

Consequently, based on the analysis of the PF, the HEA is more interesting as thermoelectrics as it bears good PF values at moderate carrier concentrations.

The electronic thermal conductivity (k_e) of the two structures as a function of the carrier concentration at the temperatures of 300 K, 500 K and 700 K is depicted in Fig. 7. The electronic thermal conductivity remains nearly constant in the low carrier concentration range (10^{17} to 5×10^{19} cm^{-3}), then it increases sharply at high concentrations. In addition, k_e decreases with the temperature at high carrier concentrations. This behavior is analogous to the influence of carrier concentrations and temperature on the electrical conductivity, owing to the linear correlation between k_e and σ[68,69]. For both structures, the electronic thermal conductivity of the n-type one is always higher than that of the p-type one. Compared to HEA[48], for both n-type and p-type structures, the electrical thermal conductivity is increased.

A note must be made regarding the approximations used in this work. Due to the high computational cost involved in determining the electron relaxation time (τ), the same value of τ has been used for both TET and ORTH as that determined for HEA. The electron relaxation time for HEA was calculated using the deformation potential theory[48]. Given the higher symmetry of the TET and ORTH structures, it is expected that approximating τ_{TET} and τ_{ORTH} with τ_{HEA} likely underestimates the relaxation times of these ordered structures compared to HEA. This underestimation may consequently lead to an underestimation of their electrical conductivity and electronic contribution to the thermal conductivity. As to the power factor, since S is not dependent on τ when determined in the frame of the relaxation time approximation, PF_{TET} and PF_{ORTH} may equally be underestimated. The extent of these reductions, however, cannot be quantified. Compared with the experimental data on the PbSnTeSe HEA compound[30-32] determined at 700 K and 6×10^{19} h/cm^3, our calculated values of the Seebeck coefficient for both the ordered and disordered structures are

in closely agreement (approximately 160 μV/K). In contrast, our estimates of the electrical conductivity, and consequently the power factor, and about half the experimental data. The reason for this discrepancy remains unclear. Indeed, the experimental electrical conductivity should be lower than the calculated one due the presence of impurities and grain boundaries. The discrepancy might be explained by an underestimated value of the electron relaxation time (τ_{HEA}) in our calculations. Anticipating the lattice thermal conductivity and figure of merit presented hereafter, our calculations show that the former about half the experimental data. Overall, integrating the ZT components yields a calculated figure of merit very similar to the experimental values.

Lattice thermal conductivity. The lattice thermal conductivity is calculated within the frame of the Green-kubo theory[70] and reads:

$$\kappa = \lim_{t\to\infty} \frac{1}{3k_B T^2 V} \int_0^t < j(t')j(0) > dt'$$

Where k_B, T and V denote the Boltzmann constant, the temperature and the volume of the system, respectively. $j(t)$ is the heat flux and the symbol $<\cdot>$ represents the ensemble average over every MD simulation. Based on the heat flux calculated using the MLFF, the heat-flux autocorrelation function (HFACF) of ORTH and TET has been obtained. Fig. 8(a) and (c) show the calculated normalized averaged HFACF at the temperature of 300 K as a function of correlation time. The HFACF is oscillating, starting from the value 1 at the origin, and then the oscillations attenuate to zero indicating that the HFACF has converged. The HFACF is then used to determine the thermal conductivity (κ_L) of ORTH and TET. Fig. 8(b) and (d) show the calculated κ_L at the temperature of 300 K as a function of correlation time. The lattice thermal conductivity is also oscillating with time but converges to a stable value, hence asserting the proper convergence of our simulations.

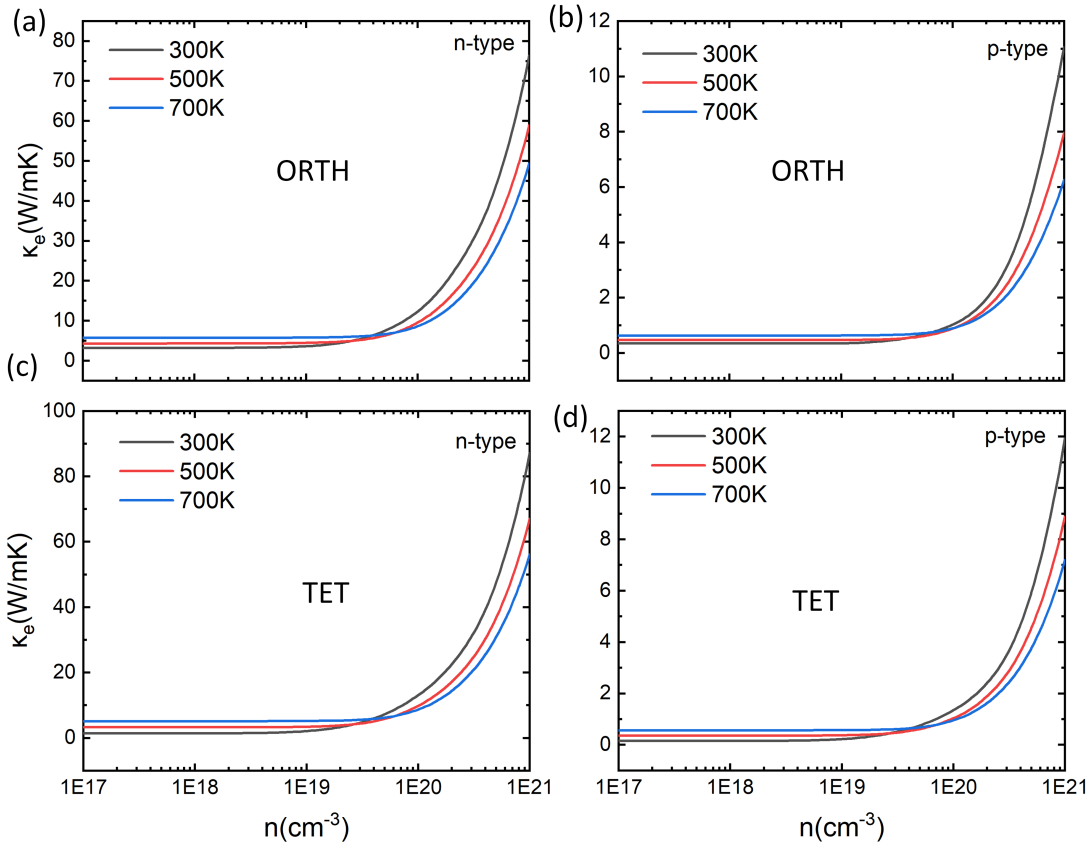

Figure 7. Electronic part of the thermal conductivity (κ_e) of ORTH (a) and (b) and TET (c) and (d) for n-type and p-type at 300 K, 500 K, and 700 K as a function of carrier concentration.

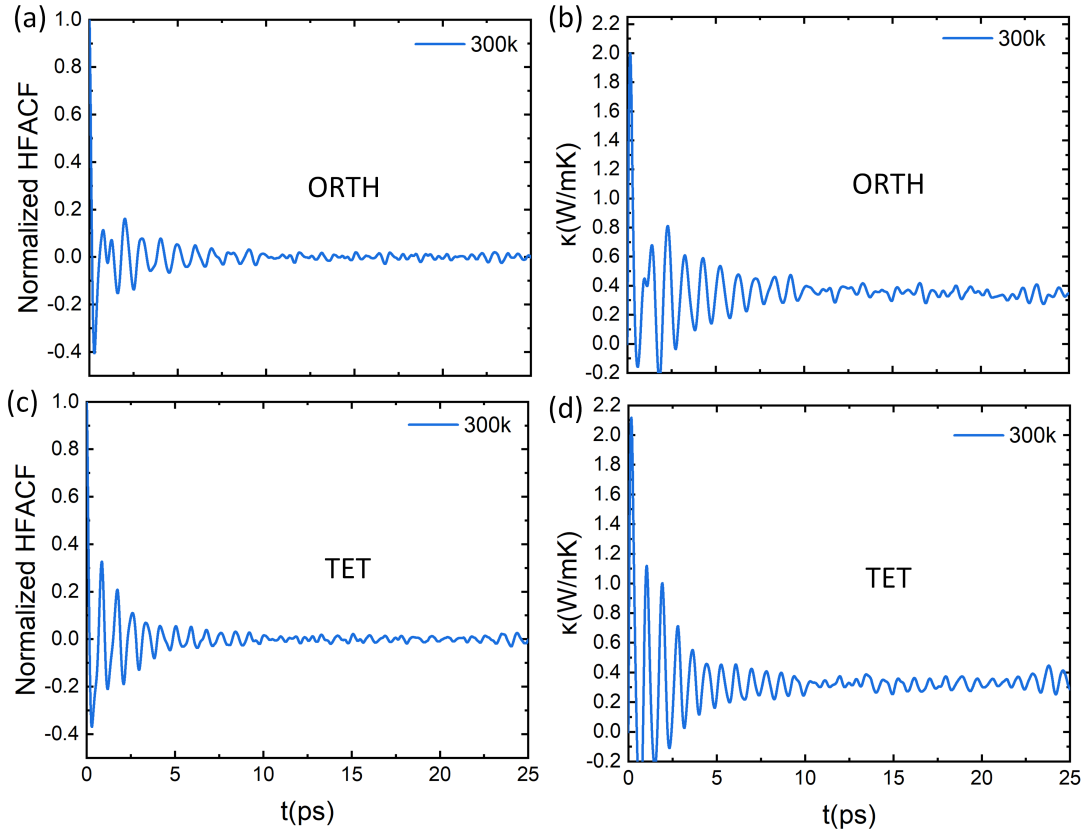

Figure 8. Lattice thermal properties at 300 K from Green-Kubo theory. Lattice thermal conductivity (κ_L) and heat-flux autocorrelation function (HFACF) normalized by its zero-time value of ORTH (a) and (b) and TET (c) and (d) as a function of correlation time at T = 300 K.

As with HEA[48], the κ_L values of TET and ORTH symmetrical structures are around 0.4 W K^{-1} m^{-1}. High-entropy alloys typically exhibit a low thermal conductivity usually attributed to their multi-element composition and high atomic mixing, which lead to strong anharmonic phonon scattering. In this study, when comparing structures with the same composition but different degrees of disorder, it is observed that there is little change in the thermal conductivity. This result, to some extent, infers that the low thermal conductivity of high-entropy alloys is primarily contributed by their multi-element composition and that the contribution of atomic disorder to the lattice thermal conductivity is relatively minor.

Fig. 9 shows the root mean square displacement (RMSD) of the atoms in the HEA, ORTH and TET structures, accumulated during the dynamics simulations. As expected, it can be seen that the shape of the RMSD curves w.r.t. the correlation time is identical. RMSD rises rapidly first, then gently and almost linearly with the correlation time. A difference is however observed in the rate of increase in the linear region. Indeed, the rates of ORTH and TET are slightly lower than that of HEA, in line with the ordering of κ_L between the three structures (0.3, 0.35 and 0.4 W K^{-1} m^{-1} for TET, ORTH and HEA, respectively). The rate of change of the RMSD curve over time may also provide insights into the diffusion properties of the atoms in the structure. The averaged self-diffusion coefficient D_0 of the atoms in the HEA is higher than those in TET and ORTH, which relates to the above-mentioned κ_L ordering. More interestingly, this finding aligns with the calculated mechanical properties reported above showing that HEA is more deformable than ORTH and TET.

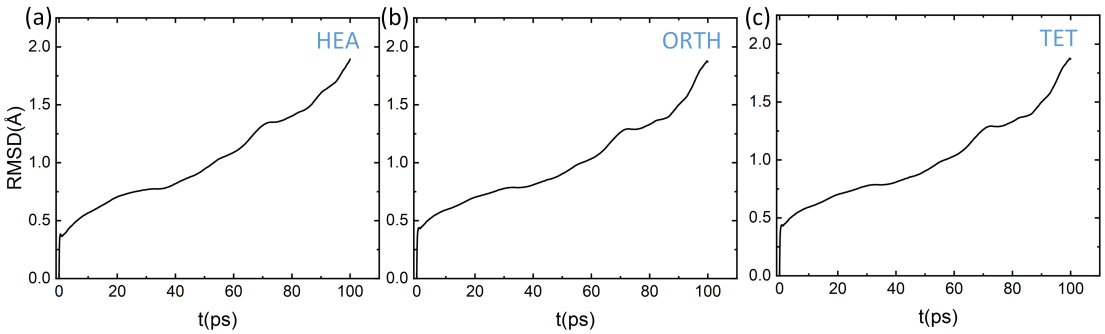

Figure 9. Root mean square displacement of atoms in HEA (a), ORTH (b) and TET (c) structures accumulated during the molecular dynamics simulations as a function of correlation time at T = 300 K.

Figure of merit. Fig. 10 shows the ZT values of the two structures (ORTH and TET) as a function of the carrier concentration at the temperatures of 300 K, 500 K and 700 K. For the p-type doping, the optimal ZT value increases as the temperature increases and the optimal value of the two

structures is almost the same around 1.1 at 700 K. For the p-type disordered structure, the optimal *ZT* value is found to be 0.75 at 700 K[48]. As the *S* values are somewhat similar in the three structures, the difference stems from the electrical conductivity and lattice thermal conductivity that are smaller and larger, respectively, in the HEA.In the case of n-type doping, except for TET at 300 K, the optimal *ZT* of ORTH and TET is smaller than that of the disordered structure[48]. At 300 K, the value of TET is much larger due to both higher *S* and σ.

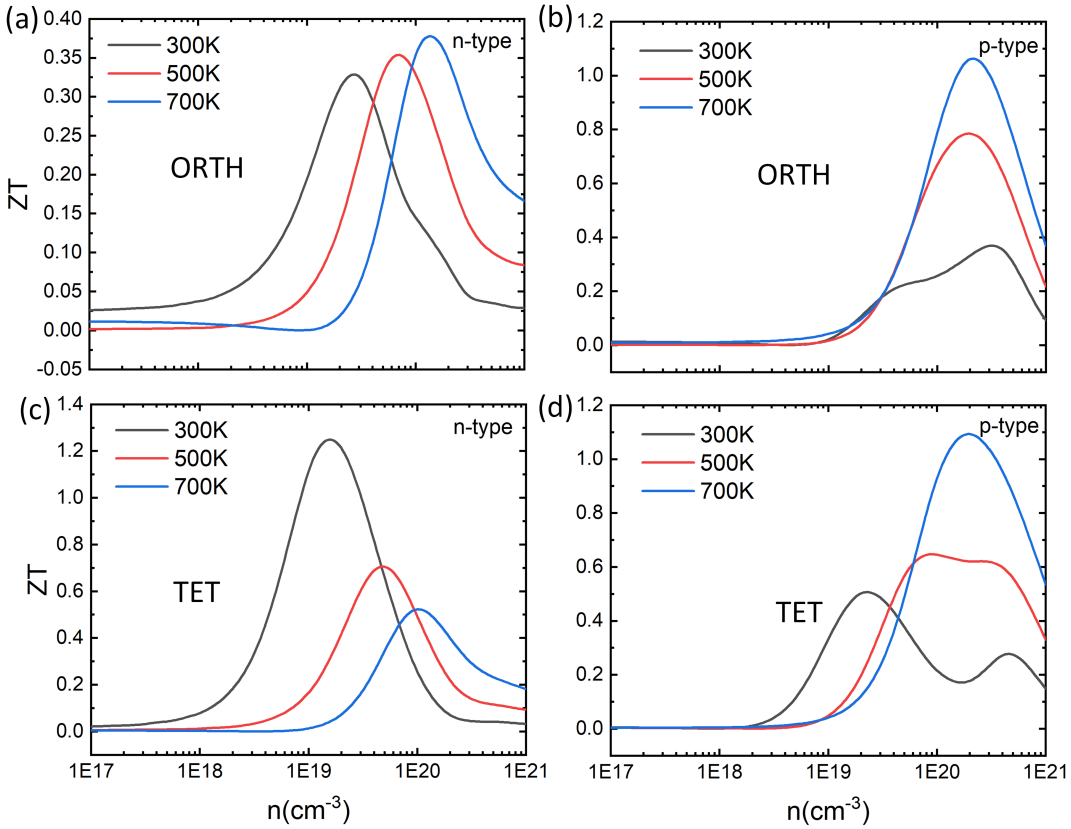

Figure 10. Figure of merit (*ZT*) of ORTH (a) and (b) and TET (c) and (d) for n-type and p-type alloys at 300 K, 500 K, and 700 K as a function of carrier concentration.

CONCLUSIONS

High-entropy alloys are characterized by a multi-element composition and extensive atomic mixing. In order to investigate the influence of disorder in HEA on thermoelectric properties and phase stability, we have built two PbSnTeSe structures with an identical composition to that of the HEA by artificially setting the atoms in the structures so that they form symmetrical structures rather than a completely random one. The so-obtained symmetrical alloys bear a tetragonal structure with space group Pmmm (TET) for one, and an orthorhombic structure with space group P4/mmm (ORTH) for the other. Then, the stability of these structures has been investigated. All the structures exhibit mechanical stability whereas only the HEA demonstrates dynamic stability and bears the lowest free energy. The multi-cell relaxation Monte Carlo simulations predict that the HEA is single phased, which is consistent with the experimental results. Subsequently, we have employed first-principles density-functional theory in combination with Boltzmann transport theory to investigate the thermoelectric transport properties of these two symmetrical structures (TET and ORTH). The results reveal that, in comparison to HEA, there is little difference in the Seebeck coefficient and the electrical conductivity is increased. The lattice thermal conductivity is barely different between the HEA and the two structures suggesting that the low thermal conductivity observed in high-entropy alloys primarily arises from their multi-element composition while the contribution of atomic disorder to the lattice thermal conductivity is relatively minor. Therefore, a potential approach to finding high-efficiency thermoelectric materials could be to consider HEAs with as many elements as stability allows.

AUTHOR INFORMATION

Corresponding Author

Marie-Christine Record: m-c.record@univ-amu.fr

Author Contributions

The manuscript was written through contributions of all authors. All authors have given approval to the final version of the manuscript. All the authors contributed equally.

Funding Sources

This work received no funding.

ACKNOWLEDGMENT

This work has been carried out under the allocation A0150806881 granted by the Grand Equipement National de Calcul Intensif (HPC resources of GENCI—France). The "Centre de Calcul Intensif d'Aix-Marseille" is acknowledged for granting access to its high-performance computing resources. The China Scholarship Council is acknowledged for supporting MX PhD thesis.

REFERENCES

(1) Jaworski, C. M.; Wiendlocha, B.; Jovovic, V.; Heremans, J. P. Combining alloy scattering of phonons and resonant electronic levels to reach a high thermoelectric figure of merit in PbTeSe and PbTeS alloys. *Energy Environ. Sci.* **2011**, *4* (10), 4155–4162.

(2) Snyder, G. J.; Toberer, E. S. Complex thermoelectric materials. *Nature Mater.* **2008**, *7*, 105–114.

(3) Biswas, K.; He, J.; Blum, I. D.; Wu, C.-I. ; Hogan, T. P.; Seidman, D. N.; Drvaid, V. P.; Kanatzidis, M. G. High-performance bulk thermoelectrics with all-scale hierarchical architectures. *Nature* **2012**, *489*, 414–418.

(4) Sootsman, J. R.; Chung, D. Y.; Kanatzidis, M. G. New and Old Concepts in Thermoelectric Materials. *Angew. Chem. Int. Ed.* **2009**, *48* (46), 8616–8639.

(5) Aoyama, I.; Kaibe, H.; Rauscher, L.; Kanda, T.; Mukoujima, M.; Sano, S.; Tsuji, T. Doping Effects on Thermoelectric Properties of Higher Manganese Silicides (HMSs, $MnSi_{1.74}$) and Characterization of Thermoelectric Generating Module using *p*-Type (Al, Ge and Mo)-doped HMSs and *n*-Type $Mg_2Si_{0.4}Sn_{0.6}$ Legs. *Jpn. J. Appl. Phys.* **2005**, *44*, 4275.

(6) Jood, P.; Ohta, M.; Yamamoto, A.; Kanatzidis, M. G. Excessively Doped PbTe with Ge-Induced Nanostructures Enables High-Efficiency Thermoelectric Modules. *Joule* **2018**, *2*, 1339–1355.

(7) Hu, X.; Jood, P.; Ohta, M.; Kunii, M.; Nagase, K.; Nishiate, H.; Kanatzidis, M. G.; Yamamoto, A. Power generation from nanostructured PbTe-based thermoelectrics: comprehensive development from materials to modules. *Energy Environ. Sci.* **2016**, *9* (2), 517–529.

(8) Deng, R.; Su, X.; Hao, S.; Zhang, Z.; Zhang, M.; Xie, H.; Liu, W.; Yan, Y.; Wolverton, C.; Uher, C.; Kanatzidis, M. G.; Tang, X. High thermoelectric performance in $Bi_{0.46}Sb_{1.54}Te_3$ nanostructured with ZnTe. *Energy Environ. Sci.* **2018**, *11* (6), 1520–1535.

(9) Naghavi, S. S.; He, J.; Xia, Y.; Wolverton, C. Pd_2Se_3 Monolayer: A Promising Two-Dimensional Thermoelectric Material with Ultralow Lattice Thermal Conductivity and High Power Factor. *Chem. Mater.* **2018**, *30* (16), 5639–5647.

(10) Shafique, A.; Shin, Y.-H. Thermoelectric and phonon transport properties of two-dimensional IV–VI compounds. *Sci. Rep.* **2017**, *7*, 506.

(11) Patel, A.; Singh, D.; Sonvane, Y.; Thakor, P. B.; Ahuja, R. High Thermoelectric Performance in Two-Dimensional Janus Monolayer Material WS-X (*X* = Se and Te). *ACS Appl. Mater. Interfaces* **2020**, *12* (41), 46212–46219.

(12) Mansoor, A.; Jabar, B.*;* Li, F.; Jamil, S.; Fasehullah, M. ; Chen, Y.-X.; Liang, G.-X.; Fan, P.; Zheng, Z.-H. Strain-Mediated Lattice Rotation Design for Enhancing Thermoelectric Performance in Bi_2S_2Se. *Adv. Funct. Mater.* **2023**, *33* (31), 2302770.

(13) Nolas, G. S.; Sharp, J.; Goldsmid, H. J. *Thermoelectrics: Basic Principles and New Materials Developments*. vol. 45, Springer Berlin Heidelberg, 2001.

(14) Tsai, M.-H. Yeh, J.-W. High-Entropy Alloys: A Critical Review. *Mater. Res. Let.* **2014**, *2* (3), 107–123.

(15) Yeh, J.W.; Chen, S. K.; Lin, S. J.; Gan, J. Y.; Chin, T. S.; Shun, T. T.; Tsau, C. H.; Chang, S. Y. Nanostructured High-Entropy Alloys with Multiple Principal Elements: Novel Alloy Design Concepts and Outcomes. *Adv. Engin. Mater.* **2004**, *6* (5), 299–303.

(16) Yeh, J.-W. Recent Progress In High-Entropy Alloys. *Ann. Chim. – Sci. Mater.* **2006**, 31, 633–648.

(17) Santodonato, L. J.; Zhang, Y.; Feygenson, M.; Parish, C. M.; Gao, M. C.; Weber, R. J. K.; Neuefeind, J. C.; Tang, Z.; Liaw, P. K. Deviation from high-entropy configurations in the atomic distributions of a multi-principal-element alloy. Deviation from high-entropy configurations in the atomic distributions of a multi-principal-element alloy. *Nat. Commun.* **2015**, *6*, 5964.

(18) Senkov, O. N.; Miller, J. D.; Miracle, D. B.; Woodward, C. Accelerated exploration of multi-principal element alloys with solid solution phases. *Nat. Commun.* **2015**, *6*, 6529.

(19) Dragoe, N. Bérardan, D. Order emerging from disorder. *Science* **2019**, *366* (6465), 573–574.

(20) Ataie, S. A.; Keshtmand, R.; Zamani-Meymian, M. R. Nano-mechanical properties of Cr-Zr-Nb-N medium entropy alloy films produced by reactive sputtering. *Intern. J. Refract. Met. Hard Mater.* **2023**, 110, 106006.

(21) Łoński, W.; Spilka, M.; Kądziołka-Gaweł, M.; Gębara, P.; Radoń, A.; Warski, T.; Łoński, S.; Barbusiński, K.; Młynarek-Żak, K.; Babilas, R. Microstructure, magnetic properties, corrosion resistance and catalytic activity of dual-phase AlCoNiFeTi and AlCoNiFeTiSi high entropy alloys. *J. Alloys & Compds* 2023, *934*, 167827.

(22) Nundy, S.; Tatar, D.; Kojcinovic, J.; Ullah, H.; Ghosh, A.; Mallick, T. K.; Meinusch, R.; Smarsly, B. M.; Tahir, A. A.; Djerdj, I. Bandgap Engineering in Novel Fluorite-Type Rare Earth High-Entropy Oxides (RE-HEOs) with Computational and Experimental Validation for Photocatalytic Water Splitting Applications. *Adv. Sust. Syst.* **2022**, *6* (7), 2200067.

(23) Detor, A.; Oppenheimer, S.; Casey, R.; Crawford, C. Refractory high entropy alloy dataset with room temperature ductility screening. *Data in Brief* **2022**, *45*, 108582.

(24) Zhang, Y.; Zuo, T. T.; Tang, Z.; Gao, M. C.; Dahmen, K. A.; Liaw, P. K.; Lu, Z. P. Microstructures and properties of high-entropy alloys. *Progress in Mater. Sci.* **2014**, *61*, 1–93.

(25) Rost, C. M.; Borman, T.; Hossain, M. D.; Lim, M.; Quiambao-Tomko, K. F.; Tomko, J. A.; Brenner, D. W. ; Maria, J.-P.; Hopkins, P. E. Electron and phonon thermal conductivity in high entropy carbides with variable carbon content. *Acta Mater.* **2020**, 196, 231–239.

(26) Wang, H.; LaLonde, A. D.; Pei, Y.; Snyder, G. J. The Criteria for Beneficial Disorder in Thermoelectric Solid Solutions. *Adv. Funct. Mater.* **2013**, *23* (12), 1586–1596.

(27) Berardan, D.; Meena, A. K.; Franger, S.; Herrero, C.; Dragoe, N. Controlled Jahn-Teller distortion in (MgCoNiCuZn)O-based high entropy oxides. *J. Alloys Compnds* **2017**, *704*, 693–700.

(28) Yamashita, A.; Goto, Y.; Miura, A.; Moriyoshi, C.; Kuroiwa, Y.; Mizuguchi, Y. n-Type thermoelectric metal chalcogenide (Ag,Pb,Bi)(S,Se,Te) designed by multi-site-type high-entropy alloying. *Mater. Res. Let.* **2021**, *9* (9), 366–372.

(29) Jiang, B.; Yu, Y.; Cui, J.; X. Liu, X.; Xie, L.; Liao, J.; Zhang, Q.; Huang, Y.; Ning, S.; Jia, B.; Zhu, B.; Bai, S.; Chen, L.; Pennycook, S. J.; He, J. High-entropy-stabilized chalcogenides with high thermoelectric performance. *Science* **2021**, *371* (6531), 830–834.

(30) Fan, Z.; Wang, H.; Wu, Y.; Liu, X.; Lu, Z. Thermoelectric performance of PbSnTeSe high-entropy alloys. *Mater. Res. Let.* **2017**, *5* (3), 187–194.

(31) Raphel, A.; Singh, A. K.; Vivekanandhan, P.; Kumaran, S. Thermoelectric performance of nanostructured PbSnTeSe high entropy thermoelectric alloy synthesized via spark plasma sintering. *Phys. B* **2021**, *622*, 413319.

(32) Raphel, A.; Vivekanandhan, P.; Rajasekaran, A. K.; Kumaran, S. Tuning figure of merit in Na doped nanocrystalline PbSnTeSe high entropy alloy via band engineering. *Mater. Sci. Semicond. Process.* **2022**, *138*, 106270.

(33) Slack, G. A. In *CRC Handbook of Thermoelectrics*, ed. DM Rowe, 1995, pp. 407–440. Boca Raton, FL: CRC Press.

(34) Shafeie, S.; Guo, S.; Hu, Q.; Fahlquist, P.; Palmqvist, A. High-entropy alloys as high-temperature thermoelectric materials. *J. Appl. Phys.* **2015**, *118*, 184905.

(35) Liu, R.; Chen, H.; Zhao, K.; Qin, Y.; Jiang, B.; Zhang, T.; Sha, G.; Shi, X.; Uher, C.; Zhang, W.; Chen, L. Entropy as a Gene-Like Performance Indicator Promoting Thermoelectric Materials. *Adv. Mater.* **2017**, *29*, 1702712.

(36) Qi, B.-C.; Xiao, Y.; Zhou, Y.-M.; Zhao, L.-D. Thermoelectric transport properties of Pb–Sn–Te–Se system. *Rare Metals* **2018**, *37*, 343-350.

(37) Hu, L.; Zhang, Y.; Wu, H.; Li, J.; Li, Y.; Mckenna, M.; He, J.; Liu, F.; Pennycook, S. J.; Zeng X.; Entropy Engineering of SnTe: Multi-Principal-Element Alloying Leading to Ultralow Lattice Thermal Conductivity and State-of-the-Art Thermoelectric Performance. *Adv. Energy Mater.* **2018**, *8*, 1802116.

(38) Riva, S.; Mehraban, S.; Lavery, N. P.; Schwarzmüller, S.; Oeckler, O.; Brown, S. G. R.; Yusenko, K. V. The Effect of Scandium Ternary Intergrain Precipitates in Al-Containing High-Entropy Alloys. *Entropy* **2018**, *20*, 488.

(39) Chen, R.; Qiu, P.; Jiang, B.; Hu, P.; Zhang, Y.; Yang, J.; Ren, D.; Shi, X.; Chen , L. Significantly optimized thermoelectric properties in high-symmetry cubic Cu_7PSe_6 compounds via entropy engineering. *J. Mater. Chem. A* **2018**, *6*, 6493

(40) Zhang, R.-Z.; Gucci, F.; Zhu, H.; Chen, K.; Reece, M. J. Data-Driven Design of Ecofriendly Thermoelectric High-Entropy Sulfides. *Inorg. Chem.* **2018**, *57*, 13027−13033.

(41) Deng, Z.; Olvera, A.; Casamento, J.; Lopez, J. S.; Williams, L.; Lu, R.; Shi, G.; Poudeu, P. F. P.; Kioupakis, E. Semiconducting High-Entropy Chalcogenide Alloys with Ambi-ionic Entropy Stabilization and Ambipolar Doping. *Chem. Mater.* **2020**, *32*, 6070−6077.

(42) Wang, X.; Yao, H.; Zhang, Z.; Li, X.; Chen, C.; Yin, L.; Hu, K.; Yan, Y.; Li, Z.; Yu, B.; Cao, F.; Liu, X.; Lin, X.; Zhang, Q. Enhanced Thermoelectric Performance in High Entropy Alloys $Sn_{0.25}Pb_{0.25}Mn_{0.25}Ge_{0.25}Te$. *ACS Appl. Mater. Interfaces* **2021**, *13*, 18638−18647

(43) Jiang, B.; Yu, Y.; Chen, H. Cui, J.; Liu, X.; Xie, L.; He, J. Entropy engineering promotes thermoelectric performance in p-type chalcogenides. *Nat. Comm.* **2021**, *12*, 3234.

(44) Jiang, B.; Yu, Y.; Cui, J.; Liu, X.; Xie, L.; Liao, J.; Zhang, Q.; Huang, Y.; Ning, S.; Jia, B.; Zhu, B.; Bai, S.; Chen, L.; Pennycook, S. J.; He, J. High-entropy-stabilized chalcogenides with high thermoelectric performance. *Science* **2021**, *371*, 830–834.

(45) Mikuła, A.; Dąbrowa, J.; Kusior, A.; Mars, K.; Lach, R.; Kubowicz, M. Search for mid- and high-entropy transition-metal chalcogenides – investigating the pentlandite structure. *Dalton Trans.* **2021**, *50*, 9560.

(46) Yamashita, A.; Goto, Y.; Miura, A.; Moriyoshi, C.; Kuroiwa, Y.; Mizuguchi, Y. n-Type thermoelectric metal chalcogenide (Ag,Pb,Bi)(S,Se,Te) designed by multi-site-type high-entropy alloying. *Mater. Res. Lett.* **2021**, *9*, 366–372.

(47) Karati, A.; Ghosh, S.; Nagini, M.; Mallik, R. C.; Shabadi, R.; Murty, B. S.; Varadaraju, U. V. Thermoelectric properties of nanocrystalline half-Heusler high-entropy $Ti_2NiCoSn_{1-x}Sb_{1+x}$ (x = 0.3, 0.5, 0.7, 1) alloys with VEC > 18. J. Alloys Compd. 2022, 927, 166578.

(48) Xia, M.; Record, M.-C.; Boulet, P. Investigation of PbSnTeSe High-Entropy Thermoelectric Alloy: A DFT Approach. *Materials* **2022**, *16* (1), 235.

(49) Ikeda, Y.; Grabowski, B.; Körmann, F. *Ab initio* phase stabilities and mechanical properties of multicomponent alloys: A comprehensive review for high entropy alloys and compositionally complex alloys. *Mater. Charact.* **2019**, *147*, 464–511.

(50) Niu, C.; Rao, Y.; Windl, W.; Ghazisaeidi, M. Multi-cell Monte Carlo method for phase prediction. *npj Comput. Mater.* **2019**, *5*, 120.

(51) Kresse, G.; Hafner, J. *Ab initio* molecular dynamics for liquid metals. *Phys. Rev. B* **1993**, *47* (1), 558–561.

(52) Podryabinkin, E. V.; Shapeev, A. V. Active learning of linearly parametrized interatomic potentials. *Comput. Mater. Sci.* **2017**, *140*, 171–180.

(53) Jinnouchi, R.; Karsai, F.; Verdi, C.; Asahi, R.; Kresse, G. Descriptors representing two- and three-body atomic distributions and their effects on the accuracy of machine-learned inter-atomic potentials. *J. Chem. Phys.* **2020**, *152* (23), 234102.

(54) Verdi, C.; Karsai, F.; Liu, P.; Jinnouchi, R.; Kresse, G. Thermal transport and phase transitions of zirconia by on-the-fly machine-learned interatomic potentials. *npj Comput. Mater.* **2021**, 7, 156.

(55) Hohenberg, P.; Kohn, W. Inhomogeneous Electron Gas. Phys. Rev. 1964, 136, B864 - B871.

(56) Kohn, W.; Sham, L. J. Quantum Density Oscillations in an Inhomogeneous Electron Gas. Phys. Rev. 1965, 137, A1697-A1705.

(57) Perdew, J. P.; Burke, K.; Ernzerhof, M. Generalized Gradient Approximation Made Simple. *Phys. Rev. Lett.* **1996**, 77, 3865–3868.

(58) Kresse, G.; Furthmüller, J. Efficient iterative schemes for *ab initio* total-energy calculations using a plane-wave basis set. *Phys. Rev. B* **1996**, *54*, 11169–11186.

(59) Kresse, G.; Furthmüller, J. Efficiency of ab-initio total energy calculations for metals and semiconductors using a plane-wave basis set. *Comput. Mater. Sci.* **1996**, *6*, 15–50.

(60) Madsen, G. K. H.; Carrete, J.; Verstraete, M. J. BoltzTraP2, a program for interpolating band structures and calculating semi-classical transport coefficients. *Comput. Phys. Commun.* **2018**, *231*, 140–145.

(61) Togo, A.; Tanaka, I. First principles phonon calculations in materials science. *Scripta Mater.* **2015**, *108*, 1–5.

(62) van de Walle, A.; Tiwary, P.; de Jong, M.; Olmsted, D. L.; Asta, M.; Dick, A.; Shin, D.; Wang, Y.; Chen, L.-Q.; Liu, Z.-K. Efficient stochastic generation of special quasirandom structures. *Calphad* **2013**, *42*, 13–18.

(63) Mouhat, F.; Coudert, F.-X. Necessary and sufficient elastic stability conditions in various crystal systems. *Phys. Rev. B* **2014**, *90*, 224104.

(64) Voigt, W. *Lehrbuch der Kristallphysik*, Vieweg+Teubner Verlag, 1966.

(65) Reuss, A. Berechnung der Fließgrenze von Mischkristallen auf Grund der Plastizitätsbedingung für Einkristalle. *J. Appl. Math. Mech.* **1929**, *9* (1), 49–58.

(66) Hill, R. The Elastic Behaviour of a Crystalline Aggregate. *Proc. Phys. Soc. A* **1952**, *65*, 349.

(67) Gong, J. J.; Hong, A. J.; Shuai, J.; Li, L.; Yan, Z. B.; Ren, Z. F. Liu, J.-M. Investigation of the bipolar effect in the thermoelectric material $CaMg_2Bi_2$ using a first-principles study. *Phys. Chem. Chem. Phys.* **2016**, *18* (24), 16566–16574.

(68) Stojanovic, N.; Maithripala, D. H. S.; Berg, J. M.; Holtz, M. Thermal conductivity in metallic nanostructures at high temperature: Electrons, phonons, and the Wiedemann-Franz law. *Phys. Rev. B* **2010**, *82*, 075418.

(69) Jonson, M.; Mahan, G. D. Mott's formula for the thermopower and the Wiedemann-Franz law. *Phys. Rev. B* **1980**, 21, 4223–4229.

(70) Baroni, S.; Bertossa, R.; Ercole, L.; Grasselli, F.; Marcolongo, A. Heat Transport in Insulators from Ab Initio Green-Kubo Theory. in *Handbook of Materials Modeling: Applications:*

Current and Emerging Materials, Eds. W. Andreoni and S. Yip, pp. 809–844, Springer International Publishing, 2020.

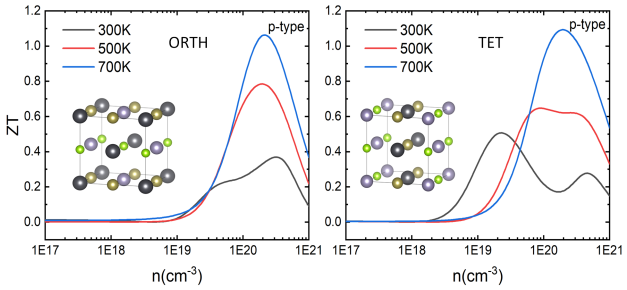

TOC Graphic